Journal of The Electrochemical Society, **153** (2) A225-A232 (2006)
0013-4651/2005/153(2)/A225/8/$15.00 © The Electrochemical Society

Liquid Water Removal from a Polymer Electrolyte Fuel Cell

F. Y. Zhang, X. G. Yang,* and C. Y. Wang*,z

Electrochemical Engine Center, Department of Mechanical and Nuclear Engineering, The Pennsylvania State University, University Park, Pennsylvania 16802, USA

Liquid water transport and removal from the gas diffusion layer (GDL) and gas channel of a polymer electrolyte fuel cell (PEFC) are studied experimentally and theoretically. In situ observations of the liquid water distribution on the GDL surface and inside the gas channel were made in an operating transparent PEFC. Liquid droplet formation and emergence from the GDL surface are characterized and two modes of liquid water removal from the GDL surface identified: one through droplet detachment by the shear force of the core gas flow followed by a mist flow in the gas channel, and the other by capillary wicking onto the more hydrophilic channel walls followed by the annular film flow and/or liquid slug flow in the channel. In the former regime, typical of high gas flow rates, the droplet detachment diameter is correlated well with the mean gas velocity in the channel. In the latter regime characteristic of low gas flow rates, liquid spreading over hydrophilic channel surfaces and drainage via corner flow were observed and analyzed. A theory is developed to determine what operating parameters and channel surface contact angles lead to sufficient liquid drainage from the fuel cell via corner flow. Under these conditions, the fuel cell could operate stably under a low flow rate (or stoichiometry) with only a minimum pressure drop required to drive the oxidizer flow. However, when the corner flow is insufficient to remove liquid water from the gas channel, it was observed that the annular film flow occurs, often followed by film instability and channel clogging. Channel clogging shuts down an entire channel and hence reduces the cell's active area and overall performance.
 [DOI: 10.1149/1.2138675]

Manuscript submitted September 6, 2005; revised manuscript received September 8, 2005.
Available electronically December 19, 2005.

Polymer electrolyte fuel cells (PEFCs) are presently regarded as a promising energy conversion system for future automobiles and stationary applications. A significant technical challenge in a PEFC is that the cell is prone to excess liquid water formation due to water production from oxygen reduction reaction (ORR) at the cathode. Liquid water may fill open pores of a gas diffusion layer (GDL), thereby blocking the transport of oxygen into a catalyst layer (CL), and may further cover the catalyst sites in the CL, rendering them electrochemically inactive. This is known as "GDL/CL flooding." Liquid water formation and subsequent flooding may also occur at low current densities under certain operating conditions, such as low temperatures and low gas flow rates, due to faster saturation of the gas phase with water vapor. If liquid water accumulation becomes excessive in a PEFC, a water lens or water band may form inside the gas channel, thereby clogging and shutting down the oxidizer flow. This latter condition is referred to as "channel flooding and clogging." In the presence of either GDL/CL flooding or channel flooding, the cell performance decreases and the longevity of PEFC materials and components suffers. Therefore, liquid water removal from a PEFC is of paramount importance for improving PEFC performance and durability.

The need for modeling liquid water formation and transport in PEFCs has long been recognized.[1-5] See the most recent review of Wang[6] for a detailed account of two-phase modeling of PEFCs. Unfortunately, experimental studies of liquid water transport in PEFCs have lagged behind until most recently, due possibly to the experimental difficulty associated with the opacity of PEFC systems and the high uniformity of temperature required to preserve the characteristics of liquid water formation and transport in PEFCs. Prior experimental efforts to probe the water distribution in an operating PEFC have included neutron radiography,[7-9] gas chromatography (GC) measurements,[10,11] and optical visualization using transparent fuel cells.[12,13] Neutron beams can penetrate through a metal fuel cell to "see" the real-time liquid water profile along a flowfield that is integrated along the cell thickness. It is noted that the neutron radiographic imaging is currently limited in both spatial (e.g., >150 μm) and temporal resolution (e.g., <30 Hz), making it difficult to capture two-phase flow phenomena in a PEFC that is transient in nature and controlled by surface forces. In addition, neutron imaging has yet to distinguish liquid water distributions on the anode and cathode, respectively. Our previous work[10,11] on water distribution measurement using a Micro GC provided unique information on the species distributions in both anode and cathode as well as water transport across the membrane, but this diagnostic tool is inapplicable to the situation where liquid water is abundant.

Optical diagnostics are capable of investigating the liquid water dynamics in a flooded cell with much higher spatial and temporal resolutions. Tuber et al.[12] visualized water buildup in the cathode channels of a transparent PEFC operating at low current densities and room temperature in order to prevent water condensation on the transparent window. Yang et al.[13] demonstrated a visualization apparatus applicable to high current densities and operating temperatures representative of automotive fuel cells. High-resolution images were shown to elucidate the dynamic behavior of liquid water on a GDL surface, including emergence as droplets at preferential locations, droplet coalescence, droplet detachment by the gas core flow, and droplet wicking onto hydrophilic channel walls. In addition, an annular film flow of liquid water sometimes turned into a water lens due to the instability of thick films, and channel clogging by the water lens followed. However, both works contained only qualitative observations.

The purpose of the present work is to quantitatively characterize liquid water removal from a PEFC, specifically from the GDL surface and gas channel. We shall experimentally and theoretically quantify the detachment diameter of water droplets emerging on the GDL, an important parameter characterizing the degree of GDL/CL flooding. It is found that at sufficiently high gas flow rates, small droplets are swept away from the GDL surface by the core gas flow, thereby resulting in a mist flow in the gas channel. This efficient mode of liquid water removal, however, requires high gas flow rate. For common air stoichiometric ratios of a PEFC, the droplet detachment diameter under the influence of gas shear force becomes comparable with the channel dimensions such that there occurs capillary wicking of liquid water from the hydrophobic GDL onto the hydrophilic channel walls. In this situation, an annular film flow results inside the gas channel, and liquid water is drained from the fuel cell via capillary flow along the corners. An analysis of liquid corner flow along a gas channel is subsequently given. Finally, when the corner flow is insufficient to drain liquid water due to either excessive water production at high current densities or to small axial pressure gradients in low gas flow, the liquid film on hydrophilic channel walls may grow thicker and unstable, eventually leading to the formation of a water lens or water band that can completely clog a gas channel.

* Electrochemical Society Active Member.
z E-mail: cxw31@psu.edu

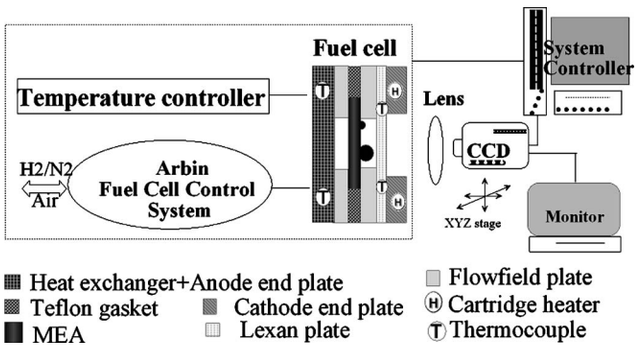

Figure 1. Schematic of the experimental setup to visualize liquid water transport in a transparent fuel cell.

Experimental

The experimental setup consists of a transparent fuel cell, a gas supply and humidification system with full control of temperature, pressure, flow rate, and relative humidity, an electronic load, a data acquisition system, and an imaging system, as shown in Fig. 1.

Transparent fuel cell.— The transparent fuel cell consisted of a membrane electrode assembly (MEA) with a 30-μm membrane of equivalent weight (EW) <1000 and catalyst loading of 0.4 mg Pt/cm^2 on each electrode. Toray carbon papers (TGPH Toray TGPH 090, 20 wt %, wet proofed with fluorinated ethylene-propylene resin were employed as GDL along with a homemade microporous layer (MPL). The GDL pore sizes are typically in the range of 10–30 μm. The MEA and GDL were sandwiched between two gold-coated, stainless steel plates (0.5-mm thick) acting as current collectors. The stainless steel plates were chemically etched to form a flowfield of seven rectangular flow channels that are each 100-mm long, 1-mm wide, and 0.5-mm deep, which are evenly separated by 1-mm wide lands for current collection. The total active area of the test cell was 14 cm^2 as defined by gaskets. One clear polycarbonate plate with antifogging coating (thus made very hydrophilic) was placed outside the cathode flowfield plate for optical access to the GDL surface and gas channels. All three surfaces (two gold-plated lands and one treated polycarbonate surface) comprising the cathode flow channels are considered very hydrophilic and impermeable as compared to the hydrophobic and permeable GDL surface. A thick end plate made of stainless steel with a window cut out was employed on the outside to compress the optical cell. To control the cell temperature accurately, a metal heat exchanger with circulating water from a constant temperature bath (Fisher Scientific) was attached on the anode side to maintain uniform cell temperature, which is critical to ensure reproducible experiments of two-phase flow and flooding in PEFCs.

In all experiments, ultrahigh purity ($>99.999\%$) hydrogen and standard dry air were used from compressed gas bottles. Two bubbler-type humidifiers were used to set desired levels of humidification in both anode and cathode inlet streams. Between the humidifiers and the test cell, electric heating tapes were wrapped around all flow lines to prevent water condensation.

Imaging system.— The visualization system consists of an objective lens assembly, a high-resolution 3-CCD video camera, a PC and image capture software, and a real-time viewing monitor with a built-in VHS recorder. The cathode of the optical fuel cell was illuminated by a high-end 150-W halogen cold light source (Intralux 6000-1) with adjustable intensities up to 320,000 fc. Fiber optic goosenecks were used to guide the light onto spots of interest along the flowfield. The charge-coupled device (CCD) camera was mounted to a XYZ microstage so that the desired location of the camera can be easily adjusted within the ranges of 10 mm in the X direction (distance between cell and camera), 180 mm in Y (height of the camera), and 300 mm in Z (along the flow field). The CCD camera was coupled with a 24× objective lens which allowed the capture of close-up images. The images could either be stored as movies on miniDV tape or captured as still digital photos on a memory card. All images were also recorded on VHS tapes simultaneously.

Results and Discussion

The effects of cathode air flow rate on the liquid water distribution and cell performance were studied in this work. In all experiments varying the air flow rate, the fuel cell was operated at the cell temperature and pressure of 80°C and 2 atm absolute with fully humidified air and hydrogen.

Liquid water distribution and cell performance.— Figure 2 shows two photographs at the same section of the test cell after running the fuel cell at 0.8 A/cm^2 for 30 min with flow velocities in the channel of 1.43 and 7.15 m/s, respectively. The view of the flowfield, close to the outlet, is 14-mm high and 16-mm long. The flow is from right to left. The lower air velocity corresponds to a flow stoichiometric ratio of 2 at the operating current density, which is commonly used in PEFC operation. The higher velocity corresponds to a stoichiometry of 10. Evidently, under common operating conditions, there exists a substantial amount of liquid water inside

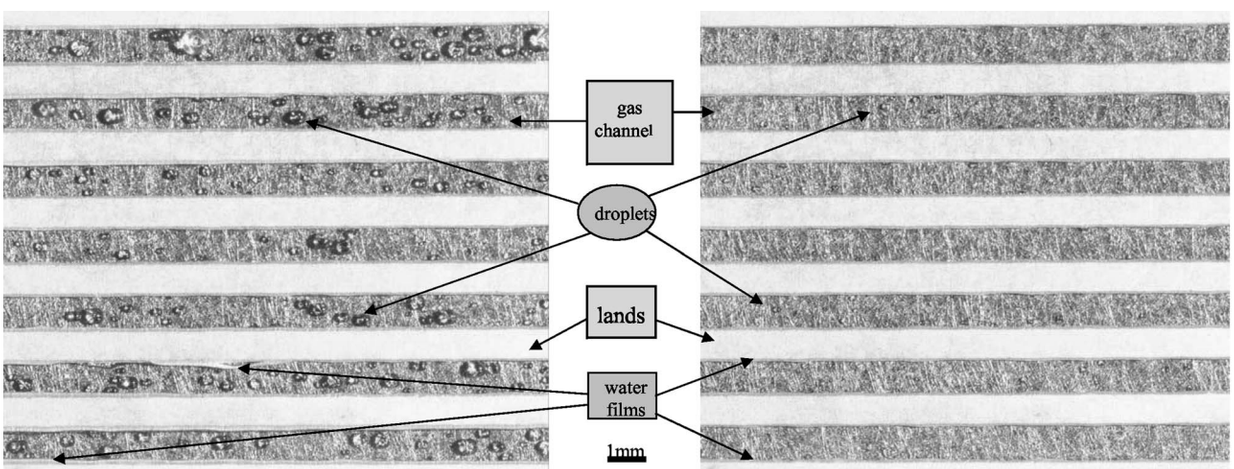

Figure 2. Photographs of the liquid water distribution for the channel gas velocity of (a) 1.43 and (b) 7.15 m/s.

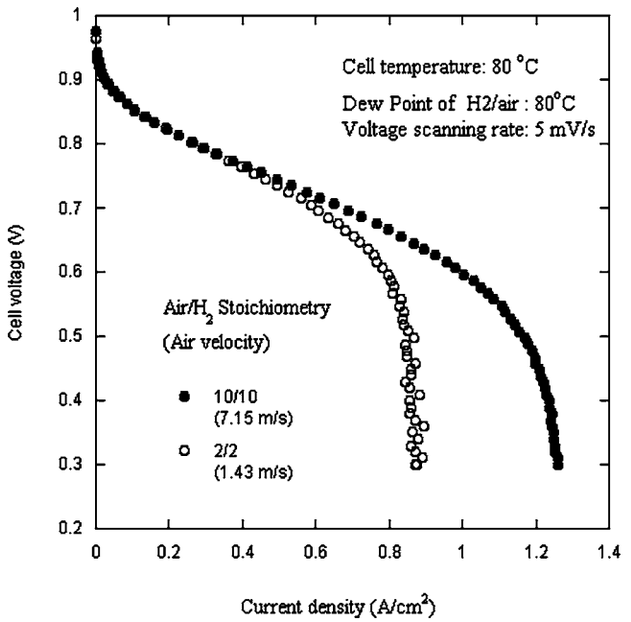

Figure 3. Polarization curves with varying gas velocities.

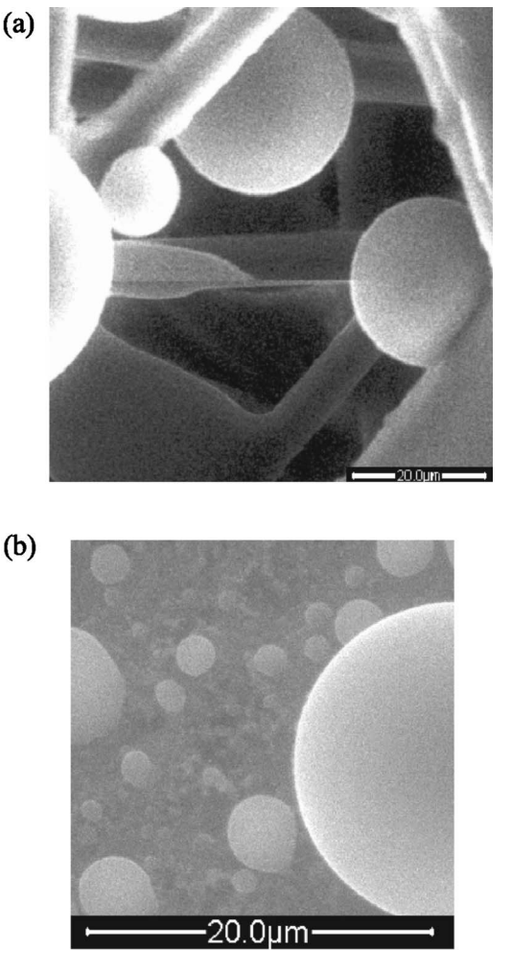

Figure 4. Environmental scanning electron micrographs (ESEM) of dropwise condensation (a) in a carbon paper GDL and (b) on a MPL.

the cathode flowfield as well as on the GDL surface. Liquid water on the GDL surface appears in the form of droplets due to the GDL's hydrophobic nature. Using a proprietary image processing tool, the fractional coverage of the GDL surface by liquid droplets was determined to be ~11% in the image shown in Fig. 2a. Large droplets are removed from the GDL surface by either the drag force exerted by the gas flow or by capillary wicking onto the neighboring hydrophilic channel walls when the droplet size becomes comparable with the channel dimension. The liquid water then appears in the form of thin films in the gas channels, as can be seen from Fig. 2a. Some of the water films are seen to be wavy due to the unstable nature of thick films. In this case, liquid water is removed from the gas channels primarily by annular flow, as in Fig. 2a.

When the air stoichiometry is increased to 10, a completely different distribution of liquid water results. As shown in Fig. 2b, there are hardly any liquid droplets attached to the GDL surface. Liquid water is apparently removed from the GDL surface by the shear force of the gas flow, followed by a mist flow through the gas channel. In mist flow tiny water droplets suspend in the gas stream and flow nearly at the same velocity as the gas, i.e., 7.15 m/s in this case. Thus, it would take ~2 ms for a droplet to pass through the field of view (16 mm in length), shown in Fig. 2b, apparently too fast to be captured clearly without a high-speed camera (i.e., >1000 fps). While this is an efficient mode of liquid water removal from the PEFC, it requires high flow and hence high parasitic pumping power to operate. A more detailed analysis of the relationship between the droplet detachment diameter and air velocity in the channel is discussed in the next subsection.

The corresponding fuel cell performance is shown in Fig. 3 in the form of polarization curves. It is clearly seen that the mass-transport limiting current density, due to liquid water accumulation inside the PEFC, is substantially improved with the higher air stoichiometry. This cell performance data confirms the significance of the liquid water distribution illustrated in Fig. 2 and to be further studied in the following.

To better understand why liquid water emerges from the GDL surface in the form of droplets and at preferential sites, an environmental scanning electron microscopy (ESEM) study was carried out to observe water condensation in GDL and on MPL surfaces. The images of dropwise condensation are shown in Fig. 4. It can be seen from Fig. 4a that liquid water beads up on hydrophobic GDL pore walls with diameters ranging from 10 to 20 μm. On the MPL surface which is more hydrophobic than the carbon paper GDL, droplets as small as 2 μm can be seen from Fig. 4b. Liquid water continually generated in the catalyst layer is transported to the GDL surface by capillary forces. Therefore, it can be said that GDL hydrophobicity results in droplet emergence and growth on the GDL surface.

Figure 5 gives several close-up photographs showing water appearance on the GDL surface, liquid water interactions with the channel walls, water drainage from the channel, and water lens formation in the gas channel. In Fig. 5a, a number of liquid droplets are clearly visible on the GDL surface at low gas velocity. At the same time, liquid water is primarily removed via the corners of the hydrophilic channel, as can be seen from the stable water films covering the channel sidewalls. Annular film flow is a dominant flow pattern under these fuel cell operating conditions of low gas flow and strong surface tension due to the small channel dimensions and strong wettabilities. According to the Concus-Finn condition,[14-16] when the channel wall contact angle θ is smaller than $(\pi/2 - \alpha)$, where α is the half-angle of the channel corner, i.e., $\theta < 45°$, liquid water wets the corners and forms a steady corner flow.

If the rate of liquid water entering the gas channel becomes high, water films appear on the channel surfaces and grow to a critical thickness which triggers an unstable or wavy shape. This is shown in Fig. 5b. There are extensive interactions between the gas and liquid phases in this regime, and the annular film flow usually transitions into a slug flow. Lobes or collars appear in the slug flow

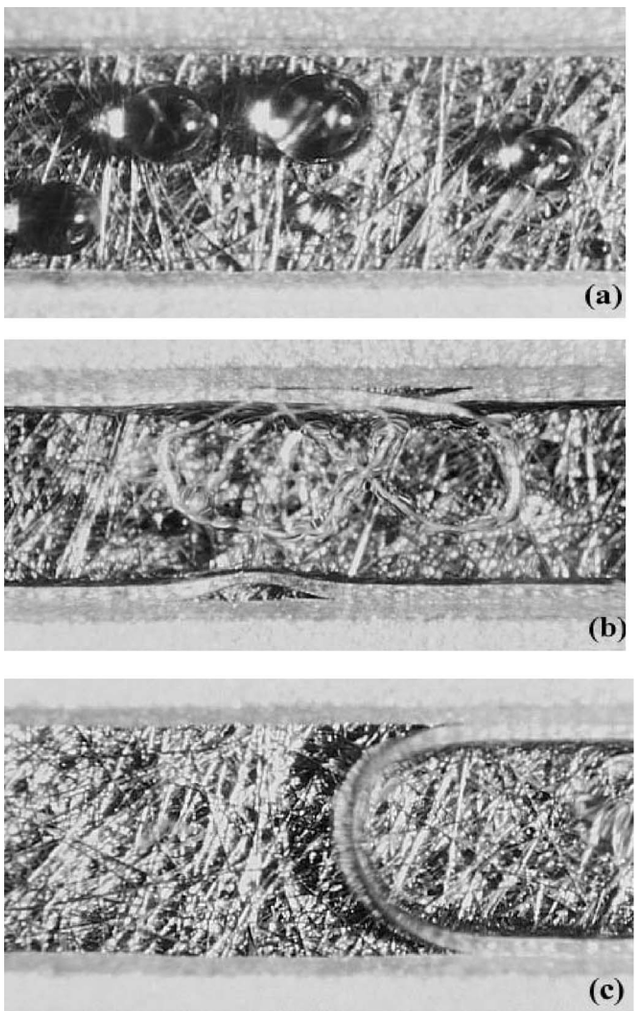

Figure 5. Close-up photographs of liquid water distribution in a PEFC: (a) corner flow with emergence of droplets, (b) annular film flow with emergence of droplets, and (c) slug flow with dynamic clogging where gas flow is from right to left.

regime and their amplitudes may lead to pinch-off of the gas flow, resulting in channel clogging as shown in Fig. 5c. Liquid slug flow results in oscillatory and increased pressure drops across the channel. Also, channel clogging shuts down entire channels and hence reduces the cell's active area for electrochemical production of current. Hence, the slug flow and channel clogging should be avoided if possible.

The three patterns of liquid water movement in the gas channel under low air velocities, namely, the corner flow, annular film flow, and slug flow, are schematically summarized in Fig. 6. The process of channel clogging by a water lens is illustrated in Fig. 7.

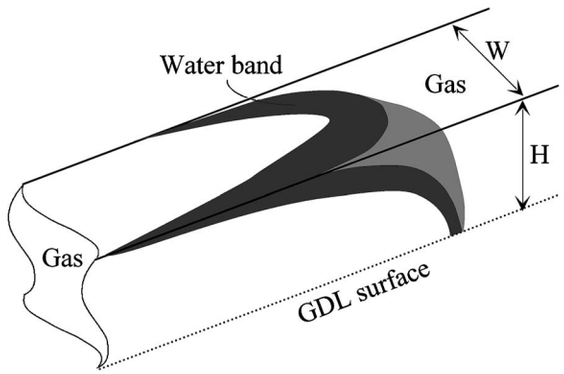

Figure 7. Three-dimensional illustration of water lens formation and channel clogging.

Liquid water removal from GDL.— Returning to liquid water removal from the GDL surface, two modes are possible, depending on the air velocity in the gas channel. One is by the drag force exerted from the gas flow when the droplet size is small and gas velocity is high. The other is by capillary interactions with the channel sidewalls when the gas velocity is low and droplets grow to a size comparable with the channel dimensions. To develop a definitive relationship between the droplet detachment diameter and air velocity in the channel, it is instructive to consider forces acting on a single droplet at the GDL surface. These are (*i*) gravitational force, (*ii*) surface adhesion force, and (*iii*) shear drag force induced by the core gas flow. The ratio of gravitational force to surface tension is given by the Bond number defined as

$$Bo = \frac{\Delta\rho g d_d^2}{\sigma} \quad [1]$$

where $\Delta\rho$ is the density difference between the liquid and the gas, g the gravitational acceleration, d_d the droplet diameter, and σ the interfacial surface tension. The maximum droplet diameter before the droplet touches and interacts with the channel bottom wall is given by a geometric relation, $2h/(1 - \cos\theta)$, where h is the channel depth and θ the GDL contact angle. In the present work, this maximum droplet diameter is 0.53 mm based on the channel depth of 0.5 mm and GDL contact angle of 150°. Correspondingly, the Bond number is estimated to be <0.06. Thus, the effects of gravity are negligible.

The surface adhesion force, which acts to hold drops onto a solid surface (GDL), is mainly governed by the surface tension, contact angle, and the diameter of the droplet. At mechanical equilibrium of a sessile droplet, the force balance on it is given by the Young equation, which gives rise to the equilibrium contact angle, θ

$$\sigma_{lv}\cos(\theta) = \sigma_{sv} - \sigma_{sl} \quad [2]$$

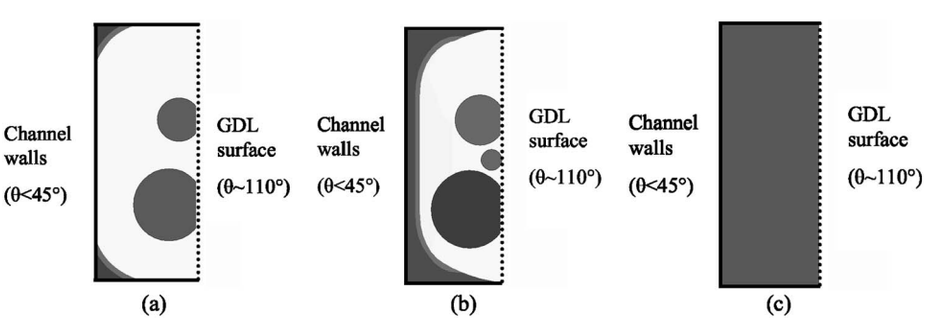

Figure 6. Various flow patterns of liquid water in the gas channel: (a) corner flow with emergence of droplets on GDL surface, (b) annular film flow with droplets on GDL surface, and (c) slug flow with transient channel clogging.

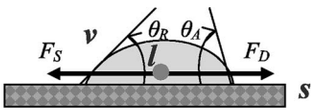

Figure 8. Schematic of force balance on a water droplet in shear flow.

As shown in Fig. 8, the adhesion force, which is a result of surface tension, is given by[17,18]

$$F_s = \sigma_{lv} d_d \sin(\theta)[\cos(\theta_r) - \cos(\theta_a)] \quad [3]$$

If advancing and receding contact angles are symmetric, such that

$$\theta_a = \theta + \Delta\theta \quad \text{and} \quad \theta_r = \theta - \Delta\theta \quad [4]$$

the total adhesion force then becomes

$$F_s = 2\sigma_{lv} d_d \sin^2(\theta)\sin(\Delta\theta) \quad [5]$$

The drag force is defined as

$$F_D = \frac{1}{2} c_D \rho V^2 A_p \quad [6]$$

where A_p is the projected area of the droplet normal to the flow direction and is calculated as

$$A_p = \frac{d_d^2}{4}\left(\theta - \frac{1}{2}\sin(2\theta)\right) \quad [7]$$

and c_D is the drag coefficient on the droplet and can be estimated from the following empirical correlation[19]

$$c_D = \frac{24}{Re}(1 + 0.1925 Re^{0.63}) = \frac{4.62}{Re^{0.37}}(1 + 5.2 Re^{-0.63}) \quad [8]$$

Here the Reynolds number, Re, is defined as

$$Re = \frac{V d_d}{\nu_g} \quad [9]$$

where V is the channel air velocity, d_d is the droplet diameter, and ν_g is the gas kinetic viscosity. The first term in Eq. 8 describes the Stoke's flow approximation for creeping flow.

It should be noted that Eq. 8 is not entirely applicable. First, although the droplet is spherical in shape, it is not a full sphere. Second, in Stoke's flow, a uniform approaching velocity is present whereas in this case, the approach velocity has a parabolic profile, starting from zero at the droplet base. Therefore, in the present derivation it is necessary to include a correction factor, K, for the drag coefficient in order to account for these two effects. Then the drag force on the droplet becomes

$$F_D = \frac{1}{2} K c_D \rho V^2 A_p \quad [10]$$

In order for a droplet to detach from the GDL surface, the drag force has to overcome the adhesion force. In this work, we define a detachment droplet diameter for which the drag force on the droplet becomes equal to the adhesion force. When the droplet diameter is bigger than the detachment droplet diameter, the drag force is larger than the adhesion force and the droplet detaches from the surface and starts to flow along with the gas stream. The detachment droplet diameter is an important design consideration for gas channel dimensions, because if the channel size is smaller than the detachment droplet diameter, the droplet will touch the channel walls before detaching from the GDL surface. In this case, the droplet will form additional solid–liquid contact, with a contact angle equal to that of the liquid water–channel surface.

Following the expressions of adhesion and drag forces, Eq. 5 and 10, respectively, the detachment droplet diameter can be calculated from

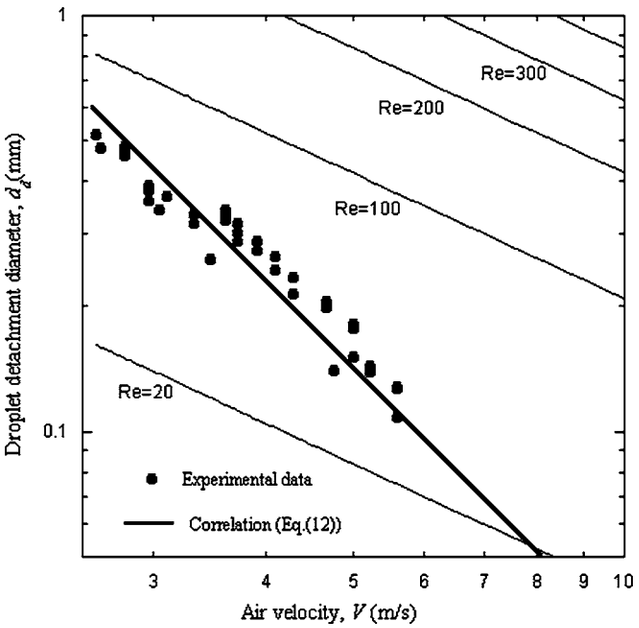

Figure 9. Correlation of droplet detachment diameter with air velocity in the channel. Linear lines representing constant droplet Reynolds number as defined in Eq. 9 are given to indicate that the Re number of experimental data ranges from 20 to 100.

$$d_d = K' c_D Re^2 \quad [11]$$

Here, all fluid (water and air) properties and surface wetting properties have been lumped into a single coefficient with the unit of micrometer, K', to be evaluated through experiments. Note also that the drag coefficient c_D is a function of the drop Reynolds number as given by Eq. 8. Substituting Eq. 8 into 11 results in

$$\log d_d = -2.59 \log V + K - 1.59 \log(1 + 5.2 Re^{-0.63}) \quad [12]$$

where the last term on the right side is not negligible in the range of Re relevant for PEFC application. Figure 9 plots the experimental relation between $\log d_d$ and $\log V$ as well as the theoretical prediction, Eq. 12. The experimental droplet diameter was measured from video clips just before droplet detachment. It is seen that the agreement is reasonably good when the coefficient K in Eq. 12 is equal to 1.0 with d_d in millimeters and V in meters per second. Keep in mind that this calibrated coefficient is applicable to carbon paper only. For other GDL materials, K varies and must be experimentally determined.

Figure 9 indicates that at an air velocity of 4.25 m/s, the droplet detachment diameter reaches 200 μm, a size that leads to possible interactions of the water droplet with the bounded walls of the channel. In this regime of droplet/wall interactions, capillary wicking of the liquid water onto the hydrophilic channel walls is a principal mechanism for liquid water removal from the GDL surface. The capillary wicking processes are composed of the droplet touching and spreading on a hydrophilic channel surface, followed by the wetting of channel corners and then by liquid drainage through the corner flow (if the Concus-Finn condition is met). These processes are shown in Fig. 10 as a sequence of still photographs obtained from a movie. It can be seen that the liquid drop spreads on the channel sidewall and wicks into the corner in less than 1 s, while a new drop emerges at the same site in about 3.5 s.

Figure 11 displays a sequence of the video frames showing droplet spreading on a hydrophilic channel wall upon impact. The spreading rate can be obtained using video clips and by measuring the spreading diameter in video frames at different times, t. Such a

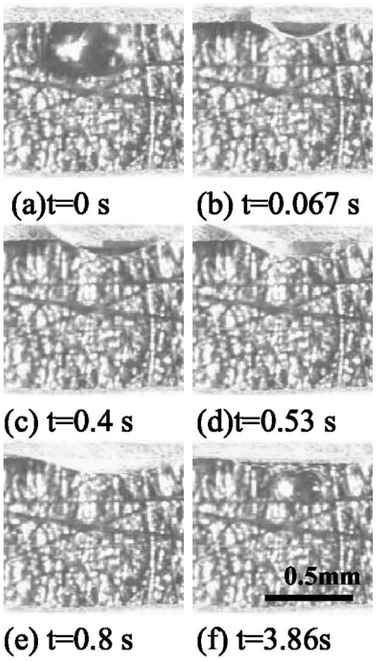

Figure 10. Sequential images of capillary interactions of a liquid droplet on GDL with a hydrophilic channel sidewall.

relation between the spreading diameter, D, or the spreading factor, D/D_o, and the time, t, is given in Fig. 12. The solid line in Fig. 12 represents a curve fit of the following equation

$$D(t) = 0.62t^{0.1} \quad [13]$$

where t is measured in seconds and D in millimeters. Based on the above equation, the local spreading rate U, given by dR/dt, is estimated to be 1.967, 0.031, and 0.0039 mm/s at the spreading time of 0.001, 1, and 10 s, respectively. Figure 12 shows that the droplet spreads from D_o to 0.7 mm in a short time before slowing down substantially. This result from the fuel cell application agrees well with Ref. 20-23. It can be inferred that liquid spreading and wicking into the channel corners is sufficiently fast if channel dimensions are around 0.7 mm.

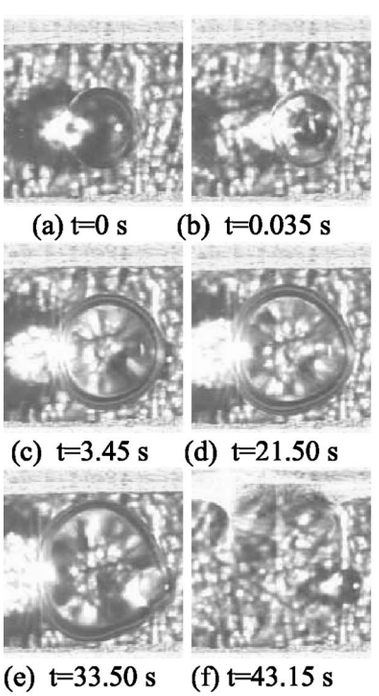

Figure 11. Sequence of photographs showing droplet spreading on a hydrophilic channel surface.

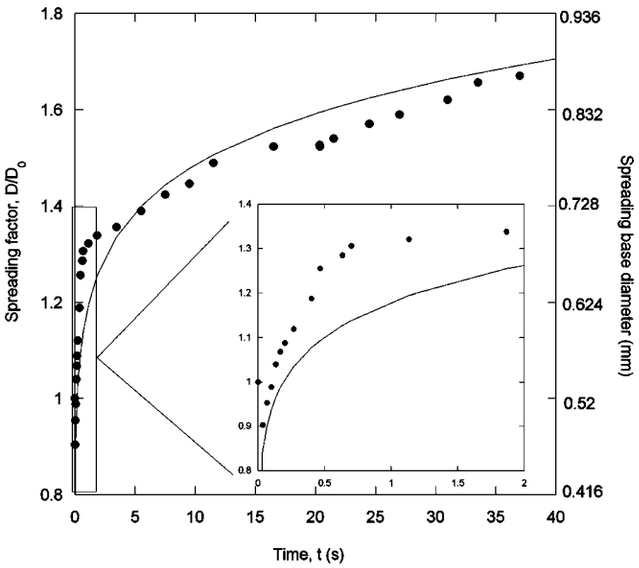

Figure 12. Experimental data of droplet spreading diameter with time.

Liquid water removal from the channel.— Under the low air velocity and strongly wetting channel surface conditions widely encountered in the PEFC application, a principal mode of liquid water removal is by corner flow. As mentioned earlier, liquid water entering a rectangular flow channel tends to imbibe into the interior corners, following the Concus-Finn condition that the channel surface contact angle, θ, and half-angle of the corner, α, satisfy the relationship $\theta < (\pi/2 - \alpha)$.

The rate of liquid drainage through steady corner flow is given by[24]

$$m_l = \frac{\rho_l R^2(-\nabla p_l)S}{\beta\mu_l} \quad [14]$$

where ∇p_l is the liquid pressure gradient that drives the corner flow, R is the mean radius of the gas-liquid interfacial curvature residing in the corner, S the cross-sectional area of liquid flow, and β a dimensionless flow resistance depending solely on the channel surface contact angle. For a square channel of dimension H, functional relationships of R and S with H for a fuel cell channel have been formulated by Sinha and Wang.[25] Using the numerically determined β from Ransohoff and Radke[24] and assuming the liquid pressure gradient equal to the gas pressure gradient (due to negligible axial variation in the gas-liquid interfacial curvature), Fig. 13 shows the drainage rate of liquid water along the corners as nondimensionalized by $(M_w/2F)I$, where M_w is the water molecular weight, F Faraday's constant, and I is the current density of the cell. The normalization factor represents the mass production rate of water from ORR at the cathode. The liquid water production rate can be simply given by

$$m_w = \frac{M_w}{2F} I\bar{L}_{2\phi} \quad [15]$$

where $\bar{L}_{2\phi}$ denotes the fractional section of the channel within the two-phase zone, or after the onset of liquid water in a general case

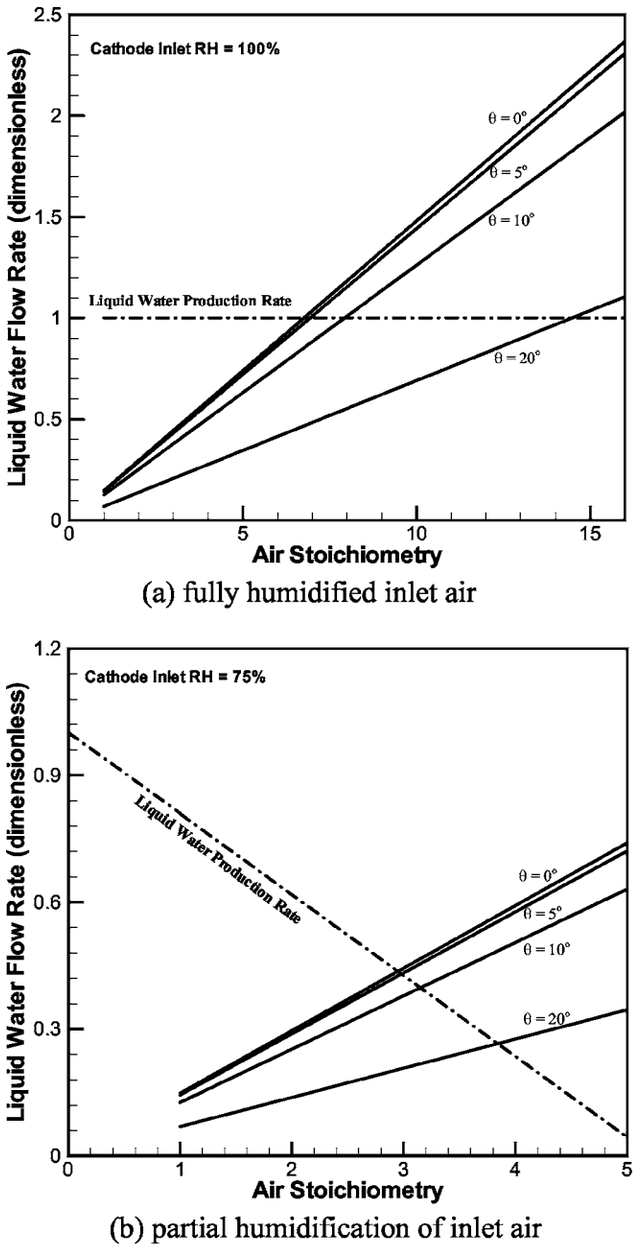

Figure 13. Drainage rate of liquid water via corner flow as compared to the liquid water production rate for the cathode inlet RH of (a) 100 and (b) 75%.

of low-humidity inlet gas. For a cathode inlet gas stream with relative humidity (RH) $<100\%$, a simple water balance yields the following relationship between $\bar{L}_{2\phi}$ and the inlet RH

$$\bar{L}_{2\phi} = 1 - \frac{\xi_c}{0.21}\frac{P_{sat}}{P - P_{sat}RH}\frac{(1 - RH)}{2 - \frac{P_{sat}}{P}} \qquad [16]$$

The liquid production rate nondimensionalized by the same factor is shown in Fig. 13 as a dashed line. For full humidification at the cathode inlet, it is constant at unity, while at *RH = 75%*, it linearly declines with the air stoichiometry, as expected. The solid lines shown in Fig. 13 represent the nondimensionalized liquid drainage rate via corner flow for various contact angles of the channel surface.

It can be seen from Fig. 13a that at the cathode inlet RH of 100%, the liquid water drainage through corner flow, driven by the gas pressure gradient along the channel, can sufficiently remove product water only when the air stoichiometry is higher than ~ 7 and when the channel surface contact angle is zero. With increasing channel contact angle, the required minimum air stoichiometry drastically increases. This is because the dimensionless flow resistance, β, increases steeply with the contact angle. One way to have the liquid drainage through corner flow balance with the liquid water production rate from the fuel cell at an appropriate air stoichiometry is to employ an inlet RH lower than 100%. The low-humidity operation reduces the amount of water production into liquid by allowing some water to evaporate into the undersaturated inlet gas. Figure 13b shows that under inlet *RH = 75%*, the water drainage rate through the channel corners can exceed the liquid water production rate at stoichiometry of 3 and 3.8 for the channel contact angles of 0 and 20°, respectively. These theoretical results indicate that drainage through steady corner flow is a promising and efficient means to remove liquid water from a fuel cell channel.

However, when the liquid drainage through stable corner flow is insufficient to remove product water, the corner flow will transition into an annular film flow with films growing on the flat surfaces of the channel. When the film thickness exceeds a critical value leading to interfacial instability, the annular film flow turns into a liquid slug flow with a water lens potentially forming to seal off an entire flow channel. In these flow regimes, both the pressure drop and cell voltage exhibit high-amplitude oscillations. A detailed study of measuring the cell's pressure drop and voltage simultaneously will be presented in a separate publication.

Conclusions

Using a transparent fuel cell featuring seven straight channels, experimental studies were carried out to delineate mechanisms of liquid water removal from the GDL surface as well as the gas channels. The following conclusions can be drawn:

1. Flow patterns of liquid water in the gas channel of a PEFC can be classified as mist flow at high air velocities, corner flow, annular film flow, and slug flow at low air velocities.
2. The mechanisms of liquid water removal from the GDL surface are by droplet detachment through the shear force exerted by the gas core flow at high air velocities (>4 m/s for the carbon paper GDL under consideration of this study) and by capillary wicking onto hydrophilic channel walls at low air velocities (i.e., <4 m/s).
3. The mechanisms of liquid water removal from a gas channel are by mist flow at high gas velocities, by a steady corner flow at low gas velocities and low water production, and by annular film/slug flow at low gas velocities and high production of liquid water.
4. Drainage through the corner flow by capillary wetting provides an efficient and low-power means of removing liquid water from gas channels and hence, it should be further investigated and optimized to meet the requirement of high water production rate in PEFCs. Maintaining very hydrophilic channel surfaces promotes liquid water drainage through corner flow.

Acknowledgments

Funding for this work from ECEC industrial sponsor is gratefully acknowledged. Thanks are also due to Puneet Sinha for providing Fig. 13.

The Pennsylvania State University assisted in meeting the publication costs of this article.

List of Symbols

A_p	area of segment part of droplet, m^2
Bo	Bond number
C_D	drag coefficient
d_d	detachment diameter of water droplet, m
D	spreading diameter of droplet, m
D_0	initial diameter of droplet before spreading, m
F	Faraday constant, C/mol
F_D	drag force, N
F_s	adhesion force, N
g	gravitational acceleration, m/s^2
H	channel dimension, m
I	current density, A/m^2
K	correction factor
$\bar{L}_{2\phi}$	fractional section of two-phase zone
M_w	water molecular weight, kg/mol
m_l	liquid water removal rate, kg/s
m_w	water production rate, kg/s
P	perimeter of contact line, m
R	mean radius of interfacial curvature, m
Re	Reynolds number
S	cross-sectional area of liquid flow, m^2
t	time, s
V	gas velocity, m/s

Greek

α	half corner angle, °
β	dimensionless flow resistance
σ	surface tension, N/m
$\Delta\rho$	density difference, kg/m^3
θ	contact angle, °
μ	viscosity, Pa s
ρ	density, kg/m^3

Subscripts

a	advancing
e	equilibrium state
l	liquid
r	receding
s	solid
v	gas phase

References

1. W. He, J. S. Yi, and T. V. Nguyen, *AIChE J.*, **46**, 2053 (2000).
2. Z. H. Wang, C. Y. Wang, and K. S. Chen, *J. Power Sources*, **94**, 40 (2001).
3. C. Y. Wang, in *Handbook of Fuel Cells—Fundamentals, Technology and Applications*, W. Lietsich, A. Lamm, and H. A. Gasteiger, Editors, Vol. 3, Part 3, p. 337, John Wiley & Sons, Chichester (2003).
4. U. Pasaogullari and C. Y. Wang, *J. Electrochem. Soc.*, **151**, A399 (2004).
5. A. Z. Weber and J. Newman, *J. Electrochem. Soc.*, **151**, A326 (2004).
6. C. Y. Wang, *Chem. Rev. (Washington, D.C.)*, **104**, 4727 (2004).
7. A. B. Geiger, A. Tsukada, E. Lehmann, P. Vontobel, A. Wokaun, and G. G. Sherer, *Fuel Cells*, **2**, 92 (2003).
8. R. Satija, D. L. Jacobson, M. A. Arif, and S. A. Werner, *J. Power Sources*, **129**, 238 (2003).
9. D. Kramer, J. Zhang, R. Shimoi, E. Lehmann, A. Wokaun, K. Shinohara, and G. G. Scherer, *Electrochim. Acta*, **50**, 2603 (2005).
10. M. M. Mench, Q. L. Dong, and C. Y. Wang, *J. Power Sources*, **124**, 90 (2003).
11. X. G. Yang, N. A. Burke, C. Y. Wang, K. Tajiri, and K. Shinohara, *J. Electrochem. Soc.*, **152**, A759 (2005).
12. K. Tüber, D. Pócza, and C. Hebling, *J. Power Sources*, **124**, 403 (2003).
13. X. G. Yang, F. Y. Zhang, A. Lubawy, and C. Y. Wang, *Electrochem. Solid-State Lett.*, **7**, A408 (2004).
14. P. Concus and R. Finn, *Proc. Natl. Acad. Sci. U.S.A.*, **63**, 292 (1969).
15. W. L. Chen, M. C. Twu, and C. Pan, *Int. J. Multiphase Flow*, **28**, 1235 (2002).
16. M. M. Weislogel and S. Lichter, *J. Fluid Mech.*, **373**, 349 (1998).
17. H. Merte, Jr., and C. Yamali, *Waerme- Stoffuebertrag.*, **17**, 171 (1993).
18. W. J. Shen, J. Kim, and C.-J. Kim, *IEEE Conference, MEMS '02*, Las Vegas, NV, USA, p. 52 (2002).
19. R. Clift, J. R. Grace, and M. E. Weber, *Bubbles, Drops, and Particles*, p. 56, Academic Press, New York (1978).
20. A. Rozhkov, B. Prunet-Foch, and M. Vignes-Adler, *Phys. Fluids*, **14**, 3485 (2002).
21. M. Wu, T. Cubaud, and C-M. Ho, *Phys. Fluids*, **16**, 7 (2004).
22. W. Liu, G. X. Wang, and E. F. Matthys, *Int. J. Heat Mass Transfer*, **38**, 1387 (1995).
23. S. Han, S. Stapf, and B. Blümich, *Phys. Rev. Lett.*, **87**, 144501 (2001).
24. T. C. Ransohoff and C. J. Radke, *J. Colloid Interface Sci.*, **121**, 392 (1988).
25. P. Sinha and C. Y. Wang, Penn State University Electrochemical Engine Center (ECEC), Report No. 2005-06 (2005).